2

In-Situ Formation of TiC Using Laser Cladding

Ali Emamian, Stephen F. Corbin and Amir Khajepour
University of Waterloo
Canada

1. Introduction

Composite materials result from the combination of two or more dissimilar materials with different physical and mechanical properties. The final product has superior properties compared to the individual components. Particles or reinforcements in different geometries, including particulates, fibres and whiskers are used in various types of matrices such as polymers, ceramics or metals. The toughness and strength of composites are thus functions of the matrix and reinforcements properties and phase morphology.

Most composites are made from a ductile matrix in which hard particles are distributed. The matrix of a composite can be a polymer, ceramic, or metal. Metal matrix composites (MMCs) are a type of composite in which ceramics, such as TiC, WC and TiB_2 with a high melting point and high hardness, are distributed in a metal matrix like Fe, Co or Ni. Fe and its alloys have attracted substantial attention of late due to their advantages over other alloys. These advantages include availability, low cost, and chemical compatibility with a wide range of steels. Al_2O_3, ZrO_2, TiN, TiC and VC are examples of hard particles used as reinforcements in metal matrices. Among these particles, TiC has sparked considerable interest because of its good wettability with Fe, high hardness and low density compared to the other components. In metal matrix composites, hard particles distributed in the matrix cause an increase in strength, stiffness, wear resistance and decreased density (Cui et al., 2007; Emamian et al., 2010c; Pu, 2008).

Different methods are used to form Fe-TiC composites. For example, Das et al. (2002) reviewed various synthesis routes of TiC-reinforced Fe-based composites such as powder metallurgy, conventional melting, casting, combustion synthesis and laser surface melting. Additionally, the authors formed TiC by a combustion synthesis method known as aluminothermy. Similarly, Jiang et al. (2000, 2007) fabricated a metal matrix composite by a casting process. Using WC and TiC as reinforcing particles, they determined that these particles are evenly distributed in the metal matrix. Unfortunately, these methods are not well suited to produce an MMC coating.

Laser cladding is an effective method which is extensively used in surface modifications of metallic materials. The highly-focused generated heat in this process results in a minimal heat-affected zone. Therefore, the process has a minimum impact on a substrate's mechanical properties. In conventional laser cladding, the majority of reinforcing phases are directly added into the coating materials (i.e., an ex-situ process). Ariely et al. (1991) carried out laser alloying of AISI 1045 steel with TiC powder fed by the dynamic blowing method. They studied the effect of changing the laser power, scan speed and feed rate on the process.

While optimum parameters significantly increase the surface hardness, some solubility of TiC in the molten Fe produces a small fraction of TiC dendrites upon re-solidification of the coating. Tassin et al. (1995) used a laser process to enhance the surface hardness of AISI 316L by adding TiC particles. As well, they added chromium carbide (Cr_2C_3) instead of TiC to augment the hardness by as much as 450 to 900 HVN.

In the ex-situ method, chemical incompatibility between the reinforcement and matrix can occur, leading to poor interfacial bonding. Different thermal properties between the composite phases (e.g., coefficient of thermal expansion, CTE) increase the risk of cracks at the poorly bonded ceramic/matrix interface in ex-situ synthesis. In contrast, in-situ laser cladding can eliminate the interface problem. The in-situ process is a method where the hard ceramic phase is formed during coating by the reaction between powder ingredients. This creates a thermodynamically stable ceramic and matrix phase with sufficient strength to transfer stresses. Therefore, the probability of crack formation and failure at the composite interface decreases. Moreover, the high solidification rate in laser cladding opens the option of controlling particle size during the evolution of reinforcement particles.

The degree of uniformity of the particle distribution throughout the matrix directly affects the degree of uniformity of the composite properties. It is therefore important to control particle distribution during a in-situ laser cladding process. The distribution of phases and the overall clad microstructure is sensitive to the relatively large number of laser cladding operating parameters. These parameters, as well as the physical phenomena which govern the in-situ process and determine the final quality of the fabricated parts, make this layer-based technique a complex process.

Du et al. (2007a, 2007b) enhanced the wear resistance and hardness of low carbon steel through the formation of TiC-VC particles in an iron matrix by laser cladding. They also achieved a similar result for TiC-TiB_2. The increase in hardness was due to carbides being distributed uniformly in the metal matrix. Wu et al (2001) increased the surface hardness with TiC_P/Ni using laser cladding.

Wang et al. (2008, 2009) increased the wear resistance of AISI 1045 steel by the in-situ synthesis of a composite coating by preplacing FeCrBSi alloy and graphite powders on the substrate surface prior to the laser surface treatment. They proposed that increasing the wear resistance might be due to the formation of a variety of in-situ carbides including TiC particles. The in-situ process was also selected by Yan et al. (1996), who formed TiC in a nickel-based alloy coating on mild steel. During the cladding process, other types of particles such as $Cr_{23}C_6$, Ni_5Si_2 and Cr_2B were formed and uniformly increased the hardness.

From the above literature review, it is clear that the in-situ formation of TiC particle metal matrix composites through laser cladding is a feasible process. Furthermore, it is widely reported that the hardness and wear resistance of the substrate can be significantly enhanced by the formation of a TiC-based composite coating. It is also clear that the TiC morphology can vary throughout the clad thickness, but no detailed or satisfactory explanation on why this happens, or what the mechanism of TiC formation is during laser cladding, has been published. This is partly due to the lack of knowledge and understanding about the relationship between clad microstructure and laser processing conditions. In addition, most researchers have focused on the use of rather complex, multi-component metal matrix powders containing various combinations of Ni, Fe, Co, Cr, B or Si. This can produce a variety of carbides other than TiC and creates complex solidification behaviour during cooling.

This chapter discusses the development of an in-situ laser cladding technique to deposit a TiC-based MMC coating on a steel substrate with no cracks and excellent bonding to the substrate and a high hardness. The approach involves feeding graphite, titanium and iron powders into a melt pool to form an in-situ clad consisting of TiC in a Fe-rich metal matrix. To study the effects of laser parameters on the quality of the clad, they are combined in two general parameters (effective energy and powder deposition density) to gain a better understanding of their roles. These parameters can help to predict the clad quality prior to conducting experiments (Emamian et al., 2009).
In order to study the effect of chemical compositions on TiC morphology, micro hardness and wear resistance of the clad, diverse chemical compositions resulting from different C:Ti ratios (i.e., 45:55 and 55:45 at%) and Fe content (i.e., 70, 60, 50 and 10 wt%) were selected for the powder composition. Additionally, several laser parameters were selected to study their effects on the clad microstructure.

1.1 Phase diagram

In this research, Fe, Ti and C are the primary components. The binary and ternary diagrams help to find the phases which are expected to appear during the process. Although the laser cladding process is a non-equilibrium process, phase diagrams are useful guides to interpret and estimate the result-ant phase formation.

1.1.1 Ti-C phase diagram

The selection of the atomic ratio forming a TiC phase is important in the formation of the TiC particles (see Fig. 1).

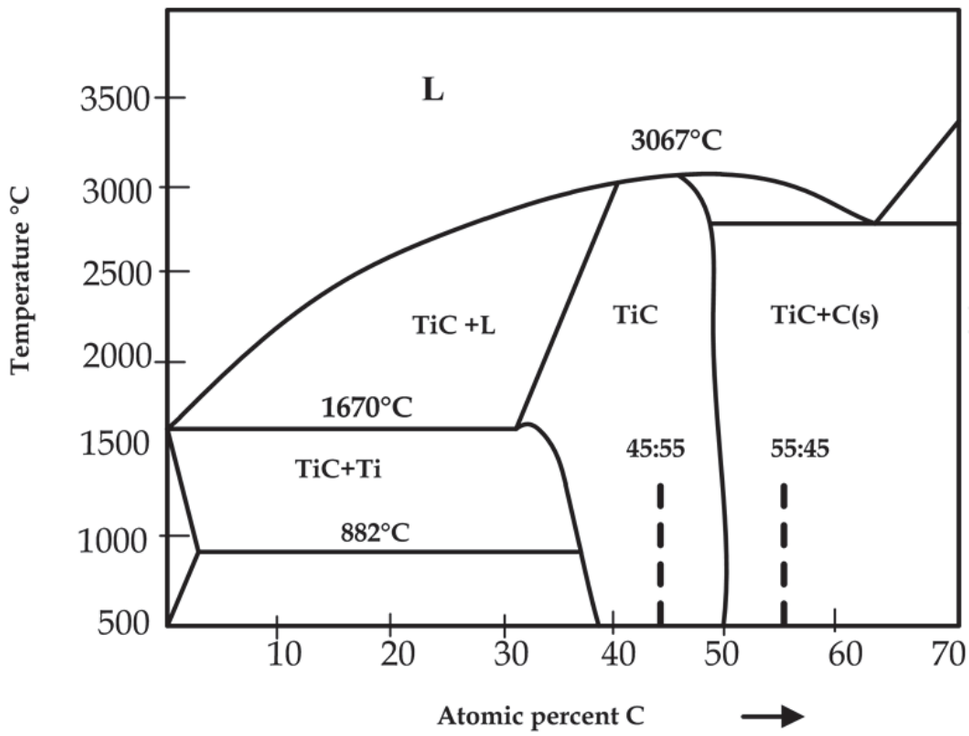

Fig. 1. Titanium-Graphite phase diagram (Hirokai, 2000)

It can be seen that TiC is stable over a wide range of composition as a intermediate phase. To avoid the formation of secondary phases such as Ti (α), Ti (ß) or C, a composition close to Ti-45%at C should be selected. For the composition study section C:Ti, the composition was changed to 55:45. Obviously, in the non-equilibrium condition phase formation can deviate from the predictions of the equilibrium phase diagram. Nonetheless, these diagrams are very useful in predicting, at least qualitatively, phase formation under non-equilibrium states.

1.1.2 Fe-Ti phase diagram

Since Fe and Ti are in contact during the melting of non-equilibrium solidification, the phase diagram below should be considered. Titanium is a ferrite stabilizer and austenite is stable in a narrow zone.

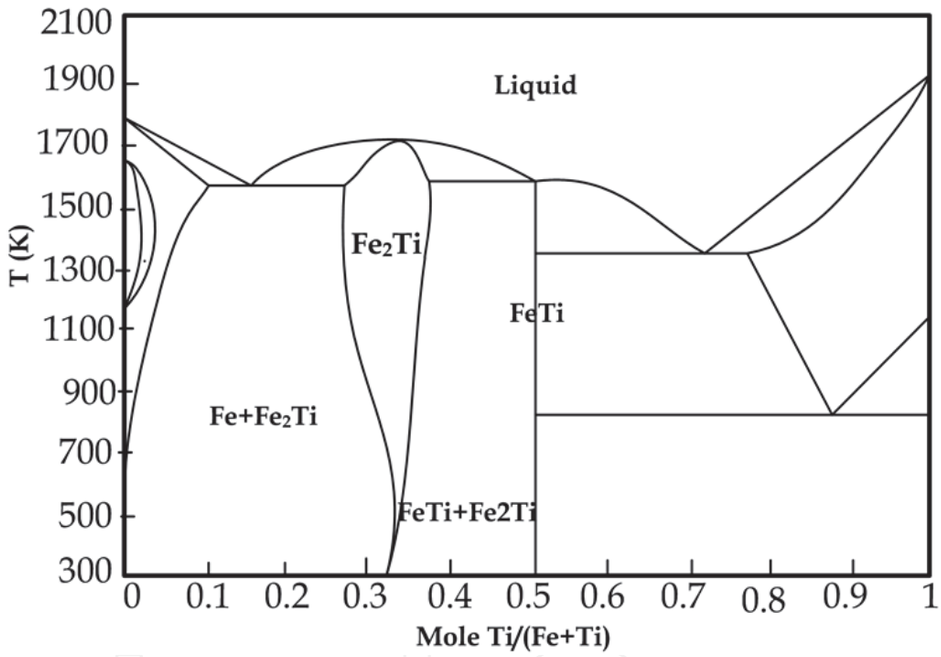

Fig. 2. Iron-Titanium Phase diagram (Hirokai, 2000)

According to Fig. 2, there are two types of intermetallics: Fe_2Ti and FeTi. Neither shows acceptable mechanical properties and hence are undesirable phases. The phase diagram of Fe-Ti shows that, by moving to the right of the phase diagram, the likelihood of both intermetallic phases being present increases. This is particularly so between the 0.3-0.5 mole fractions of titanium, where both intermetallics are in equilibrium. The goal is to form a metal matrix composite and decrease the chance of an intermetallic formation.

1.1.3 Thermodynamics of formation

Phase transformation calculations indicate that it is highly probable to have TiC particles instead of any other carbide such as Fe_3C in an in-situ TiC-Fe cladding. Fe_3C is one of several compositions which can be formed in the melt pool. The following thermodynamic equations provide information about the reactions (Dubourg & St-Georges, 2006):

$$[Ti] + [C] = <TiC> \quad \Delta G = -139,0461.31 + 98.96\ T \ \text{j/mole} \tag{1}$$

$$3Fe_{(l)} + <C> = <Fe_3C>, \quad \Delta G = -53416 + 55.68\ T \ \text{j/mole} \tag{2}$$

The equations prove that the Gibbs free energy of TiC formation is more negative than that of Fe_3C. Therefore, the probability of Fe_3C formation is lower than TiC. Although the equations are useful in equilibrium conditions, they are still useful to predict the formed phases. Moreover, it can be seen in the next chapter that there are no results to confirm the presence of Fe_3C.

2. Experimental set-up

In the experiments, AISI 1030 medium carbon steel is chosen as the substrate, with 0.28-0.34 C, 0.6-0.9 Mn, P less than 0.04, and S less than 0.05 in wt%. The substrate dimensions on which the claddings are deposited are 100×30×6.35 mm. Prior to laser cladding, the substrates are shot-blasted and rinsed with ethanol, followed by acetone.

Mixtures of Ti, graphite, and Fe powder are fed into a melt pool formed by the laser using a Sulzer Metco (TWIN 10-C) powder feeder. The ratio of C: Ti is 45:55 at %C and Ti-55 at %C. A three-digit code is considered for powder compositions. The first digit stands for Fe percentages (7 for 70) and the next two digits are the C:Ti ratios in atomic percentages (i.e., 45 or 55%). In the first two sections presented below, the powder composition was set at Ti-45% at C (745). In the composition study section, the remainder of the samples are studied (i.e. 755, 655, 555, 155). Table 1 presents the chemical compositions of powders which were studied in this chapter.

Mixtures of the powders are pre-cursors, with 99.5% purity; a 40 μm maximum powder size is further mixed with 98% purity Fe powder. To obtain a homogeneous distribution, all powders are blended for four hours at 300 rpm in a quarter-filled jar of 165×60 mm with a milling media of glassy balls where the ball-to-powder-size ratio is 20:1.

Sample group code	Fewt %	Ti wt%	C wt%	Fe at%	Ti at%	C at%
Group 745	70	25	5	57	24	19
Group 755	70	23	7	55	20	25
Group 655	60	31	9	44	26	30
Group 555	50	38	12	33	30	37
Group 155	10	69	21	5	43	52

Table 1. Chemical composition of investigated powders

An IPG fiber laser model YLR-1000-IC operating in continuous mode with a maximum power of 1 kW is used to produce a series of single-clad tracks. The diameter of the laser beam spot size on the workpiece (WP) surface is fixed at 2.5 mm. The laser machine is integrated with a five-axis CNC vertical machining centre to control the velocity of the WP. To protect the melt pool from oxidation, Argon shielding gas is supplied through a nozzle at 10 $Lmin^{-1}$.

The specimens are sectioned for micro-structural examination in a longitudinal direction. The samples are prepared using SiC grit paper with grit sizes ranging from 240 to 2400 and polished with diamonds from 6 microns to 1 micron. Afterwards, the samples are placed in an ultrasonic bath to remove any surface contaminants and then rinsed with alcohol and air dried.

A LEO SEM with 20keV is used to examine the microstructure and morphology of the phases formed during cladding. SEM is selected to determine the quality of the clad deposit (i.e., bonding to the substrate) and to determine the in-situ TiC particle morphology. The working distance is 9-14 mm and the vacuum system is set at 1.53e-0.005 mBar. Different magnifications are used to capture the microstructure. The mounting material used was conductive in order to prevent charging during sample observation.

The micro-hardness at different depths from the substrate-clad interface is measured using a Vickers micro-hardness tester, and the average of three hardness measurements is reported.

A low magnification EDS analysis of the whole longitudinal section of the clads helps to measure the Fe percentage to calculate the dilution. Further, an XRD analysis is performed with a Rigaku AFC-8 diffractometer.

Clad heights were measured by a caliper vernier. Specifically, measurements were made at the middle of the clad which normally were uniform in height. Clad height was also measured using scale bars in low magnification SEM images.

3. Laser processing conditions

The laser process parameters to determine the optimum laser cladding conditions are given in Table 2. Initial experiments were held at a constant powder feed rate of 8 g/min while systematically increasing the work piece (WP) scan speed from 2,4 to 6 mm/s. Each scan speed was explored at laser powers from 250 to 650 W (i.e., samples 1 to 9). Visual inspection of the formed clad tracks revealed that, for the power setting, a scan speed of 6 mm/s was required to produce a clad deposit.

In the second series of experiments (samples 10 to 13), the scan speed was increased from 6 to 16 mm/s while fixing the laser power and powder feed rate at 650 W and 8 g/min., respectively. Again, a clad deposit was produced in each case (except at the highest scan speed) but no bonding with the substrate occurred.

In an effort to create a clad/substrate bond, the laser power was further increased to 700 and 800 W while fixing the scan speed at 6 mm/sand using powder feed rates of 4 and 8 g/min (samples 14 to 17). Partial bonding of the clad to the substrate occurred in these cases. For example, at the higher powder feed rate, the clad adhered to the substrate immediately after cladding but detached during complete cooling. For the 4 g/min feed rate, clads remained attached to the substrate but were easily removed upon application of a small force by hand. Lowering the WP scan speed to 4, 3 or 2 mm/s (i.e., samples 18-20) did not rectify this situation.

In the final series of experiments, the laser power was increased to 900 W while the powder feed rate was at 4 or 8 g/min and the scan speed was at 6 or 8 mm/s. A laser power of 1000 W was also used with a scan and powder feed rate of 4 mm/s and 4 g/min, respectively. Visual examination of these clad tracks revealed that in all cases a clad deposit was produced and was well bonded to the substrate.

3.1 SEM results

SEM is selected to determine the quality of the clad deposit and bonding with the substrate and to find out if in-situ TiC particles are formed. For this investigation, samples which indicated a good clad deposit but no bonding with the substrate (i.e., samples 3 and 9) and a successful clad deposit (i.e., samples 23 and 24) were chosen.

However, none of these processing conditions were able to create a bond between the clad deposit and substrate.

Fig. 3 illustrates an SEM back scatter image of a typical region from the un-bonded clad deposit sample 9. It is clear that the clad microstructure consists of a matrix in which a relatively high volume fraction of uniformly dispersed particles are present. The size of these particles ranges from approximately 1 to 7 μm.

No	Power (W)	Scan Speed (mm/s)	Feed Rate (g/min)	Effective Energy (J/mm^2)	Powder Deposition Density (g/mm^2)	Observation
1	250	2	8	50	0.027	No Bond-No Clad
2	250	4	8	25	0.013	No Bond-No Clad
3	250	6	8	17	0.009	No Bonding-Formed clad
4	400	2	8	80	0.027	No Bond-No Clad
5	400	4	8	40	0.013	No Bond-No Clad
6	400	6	8	27	0.009	No bonding-Formed clad
7	650	2	8	130	0.027	No Bond-No Clad
8	650	4	8	65	0.013	No Bond-No Clad
9	650	6	8	43	0.009	No Bonding-Formed Clad
10	650	8	8	32	0.007	No Bonding-Formed Clad
11	650	10	8	26	0.005	No Bonding-Formed Clad
12	650	12	8	22	0.004	No Bonding-Formed Clad
13	650	16	8	16	0.003	No Bond-No Clad
14	700	6	8	47	0.009	Partial bonding with substrate melting
15	700	6	4	47	0.004	Weak bond-Removable Clad
16	800	6	8	53	0.009	Partial bonding with substrate
17	800	6	4	63	0.004	Weak bond-Removable Clad
18	800	2	8	160	0.027	No bonding-Formed Clad
19	800	3	8	106	0.018	No bonding-Formed Clad
20	800	4	4	80	0.007	Partial bonding with substrate
21	900	6	8	60	0.009	Successful Clad
22	900	8	8	45	0.007	Successful Clad
23	900	6	4	60	0.004	Successful Clad
24	900	8	4	45	0.003	Successful Clad
25	900	4	4	90	0.007	Successful Clad
26	1000	4	4	100	0.007	Successful Clad
27	1000	4	4	100	0.007	Successful Clad

Table 2. Results and Observation

Fig. 3 also illustrates a higher magnification image of a eutectic structure in grain boundaries of the matrix of sample 9 (i.e. region 2). Table 3 reports a typical EDS analysis performed on the dark grey dispersed particles and regions 1 and 2 of the matrix. The high Ti content of the particles is consistent with TiC particles. The majority of the matrix is a very Fe-rich phase with slightly elevated Ti concentrations in region 2. The very small black particles in Fig. 3 were too small to obtain reliable EDS analysis.
Carbon was not included in the analysis due to inaccuracies in its inclusion in a quantitative analysis.

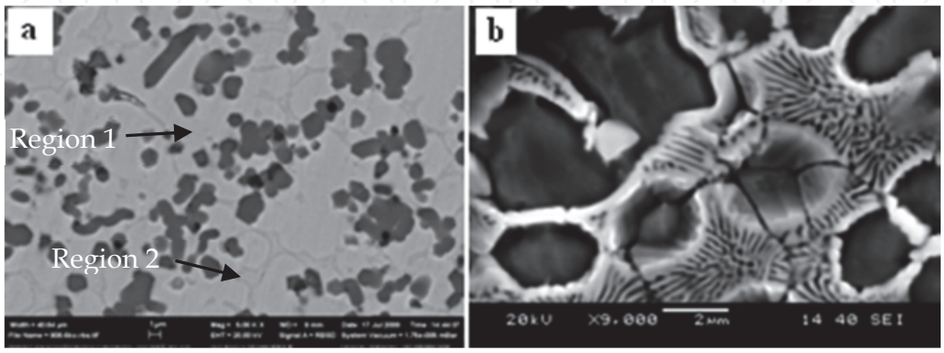

Fig. 3. BSE image of sample 9 a) distributed black particles in individual and longitudinal shape in matrix of un-bonded clad b) High magnification of Region 2 Eutectic structure of Fe-Fe_2Ti

Region	Ti conc.(wt%)	Fe conc.(wt%)
Dark grey particles	95.2	4.8
Region 1	8.7	91.3
Region 2	16.5	83.5

Table 3. EDS analysis of phases in sample 9

Fig. 4 shows a high magnification image of the two phase microstructure of sample 23. The microstructure consists of a high volume fraction of fine (i.e., < 2 μm) particles dispersed in a matrix. As with Table 3, EDS analysis confirmed that the dark grey particles are Ti-rich, whereas the matrix is Fe-rich.

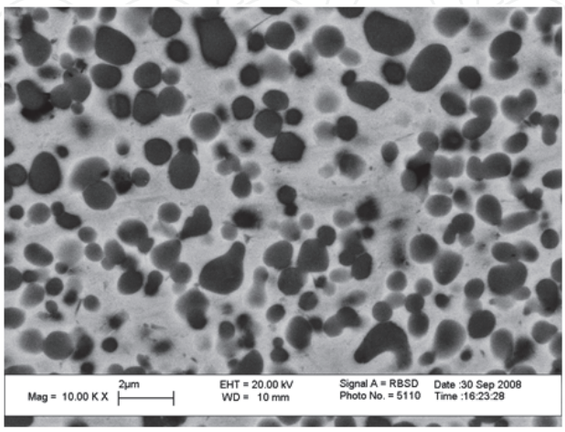

Fig. 4. BSE image-distributed black particles in matrix of a one layer clad (sample 23)

Fig. 5 shows a longitudinal section of sample 24 which confirms a uniform distribution of Ti-rich particles in an iron-rich matrix. However, in some areas, such as those labeled region A, larger black particles exist. Qualitative EDS analysis of the particles, which included carbon in the analysis, indicated a 95 wt% carbon composition with the balance as Ti and Fe. Note that the black particle in the centre of the image is surrounded by the Ti-rich grey phase. An EDS analysis of this region reveals an approximately 95 wt% Ti: 5 wt% Fe composition.

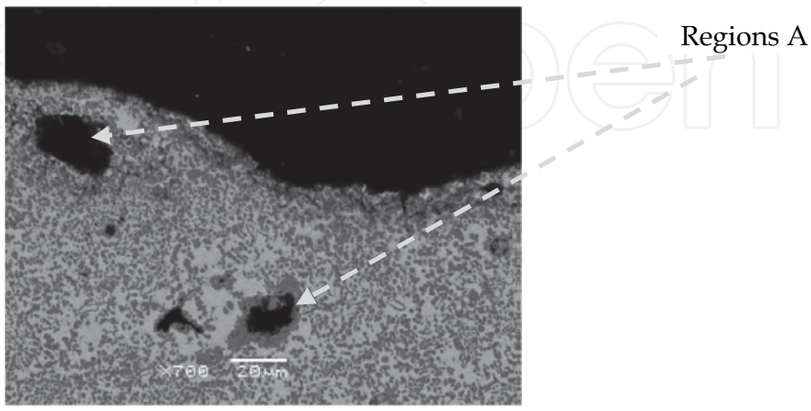

Fig. 5. Sample 24 TiC distributions

3.2 XRD results

XRD analysis was performed on samples 9 (un-bonded clad) and 23 (one layer clad). The XRD spectrums for these samples are shown in Fig. 6.

Fig. 6 depicts the XRD result for the un-bonded clad. According to this graph, TiC, Fe_2Ti and iron-titanium solid solution exist in the clad. Since there is no bonding with the substrate, dilution does not contribute to the results.

The X-ray diffraction pattern for a one layer clad is plotted in Fig. 6 and confirms the presence of the iron-titanium solid solution and TiC in the clad zone. It is worth noting that the intermetallic phase (Fe_2Ti) did not appear in the diffraction peaks of the clad coating, in contrast to the result for the un-bonded case.

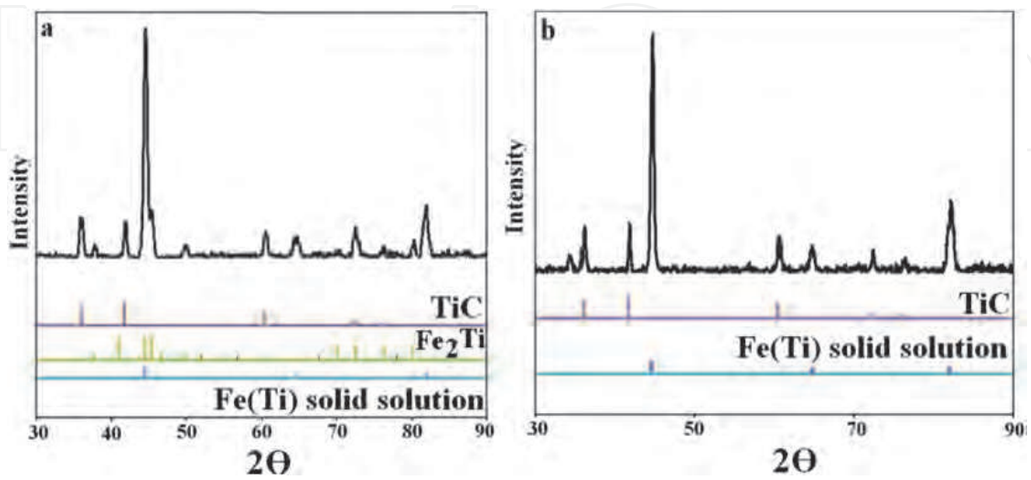

Fig. 6. XRD result of a) un-bonded clad (sample 9) and b) one layer clad (sample 23)

3.3 Further laser process/clad development and analysis

From the data in Table 2, it is clear that laser power scan speed and powder feed rate all play a vital role in clad formation, bonding, and clad quality. From the table, we can see that increasing the power increases the probability of forming a high quality clad. However, it is not the only effective parameter. In any period of time, the laser energy must provide sufficient heat to melt a given volume of the substrate as well as the incoming powder stream. This will be determined not only by the laser power but also the work piece (WP) scan speed, and powder feed rate. Two combined parameters (i.e., the effective energy per unit area (E_{eff}) and the powder deposition density (*PDD*)) are needed in order to analyze the influence of these three parameters.

Effective energy is defined as the parameter which provides a measure of the delivered energy to the process by the laser. This energy is principally responsible for melting the substrate surface and powder and can be defined by computing (Emamian et al., 2009, 2010a).

$$\text{Energy per unit area (J/mm}^2\text{)} = P/(V.D) \tag{3}$$

where P is the laser power, V is the scan speed of WP, and D is the laser spot size in *mm*. Therefore the units of effective energy are W ($mm^{-2}s^{-1}$) or Jmm^{-2}.

The powder deposition density (*PDD*) is introduced as (Emamian et al., 2010a, 2010b):

$$\text{Powder deposition density (g/mm}^2\text{)} = R/(V.D) \tag{4}$$

where V and D have the previous meaning, R is the powder feed rate in g/min, such that the powder deposition density (*PDD*) has units of g/mm^2. Table 2 reports these calculated parameters for each of the laser conditions. Fig. 7 plots the data where *PDD* is the x-axis and (E_{eff}) is the y-axis.

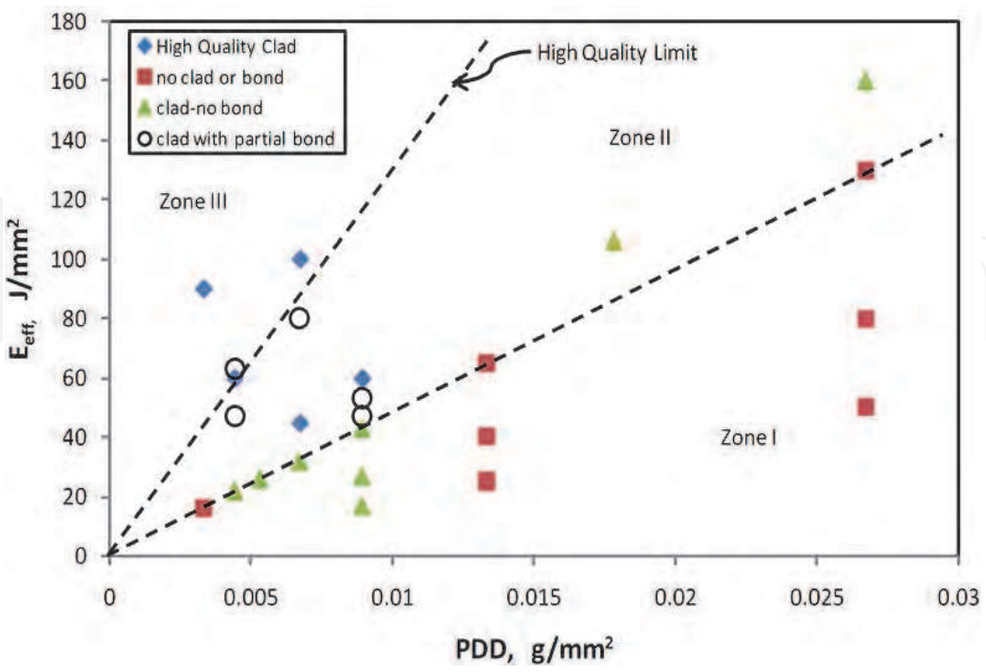

Fig. 7. Effective energy versus powder deposition density

As seen in Fig. 7, low E_{eff} and high *PDD* values leads to no clad deposit formation or bonding with the substrate. (i.e., Zone I). While increasing the E_{eff} and reducing *PDD* leads to the formation of a clad deposit, it is not bonded to the substrate (i.e., Zone II). Finally, high effective energy along with lower powder deposition density leads to the formation of a dense clad deposit which is well bonded to the substrate (i.e., Zone III). Therefore, to achieve an acceptable clad quality, effective energy and powder deposition density should be adjusted for Zone III. This graph helps us to predict the proper parameters to create an acceptable clad prior to conducting any experiment.
To further explore the predictability of this figure, a range of clad conditions which lie close to the boundary line between Zones III and II were chosen and the clad experiments completed. These conditions are discussed in the next section. All of the conditions produced a clad deposit that could not be removed from the substrate, indicating good bonding. Metallographic examination of these samples was completed to further analyze clad quality and microstructure.

3.4 TiC formation and morphology

In this section, the TiC formation mechanism is explained based on observations and phase diagrams. This explanation can be followed in two steps–namely, melting and solidification during laser cladding.
In order to explain the TiC morphology formed during laser cladding, the melting stage of the process must first be considered. When the powder mixture enters the laser beam, the powder will rapidly heat up (Fig. 8a). The melting points of pure Fe, Ti and C (or graphite) are 1538, 1668 and 3400 °C, respectively. Given the relative melting temperatures of the pure powders, it is reasonable to assume that Fe melts first, creating a liquid phase that spreads and surrounds the Ti and graphite powders (e.g., Fig. 8b). The interaction of the elements of the powder stream will cause the formation of a ternary mixture. Fig. 9 presents the liquidus surface projections for the entire ternary C-Fe-Ti composition. The actual ternary composition of the powder mixture deposited on the 1030 steel substrate is indicated by the black dot (745 PC) in Fig. 9. From these indicators, it is clear that both Ti and C have significant solubilities in the Fe-rich liquid phase and that this solubility increases with an increase in temperature. It is also clear from Fig. 9 that the Fe-rich liquid phase will be in equilibrium with solid TiC. Therefore, alloying Fe with Ti and C actually creates a ternary liquid through the gradual dissolution of the Ti and graphite powders.
In addition, a TiC layer will form between this ternary liquid and the original graphite particles in order to establish the required phase equilibrium. As the clad temperature increases, dissolution of the solid phases will continue as the solubility of Ti and C in the liquid increases. Also the growth of the TiC phase toward the graphite core will increase (e.g., Fig. 8-c). Evidence for the microstructure depicted in Fig. 8-c is presented in Fig. 5 , which illustrates graphite particles surrounded by a TiC layer.
The next stage in clad microstructural development largely depends on the peak temperature induced by the laser. If the peak melt pool temperature exceeds the liquidus temperature of the ternary composition, all of the TiC/C particles will dissolve into the melt, creating a completely liquid melt pool. If no dilution by the substrate is assumed, then it can be stated that the liquidus temperature of the clad melt pool for composition of 745 is 2345 °C. If the peak melt temperature is less than the liquidus temperature of the melt pool clad (e.g., in the presence of Fe substrate dissolution), then a semi-solid mixture will persist where the solid graphite particle core will eventually convert through the further development of the diffusion couple to TiC.

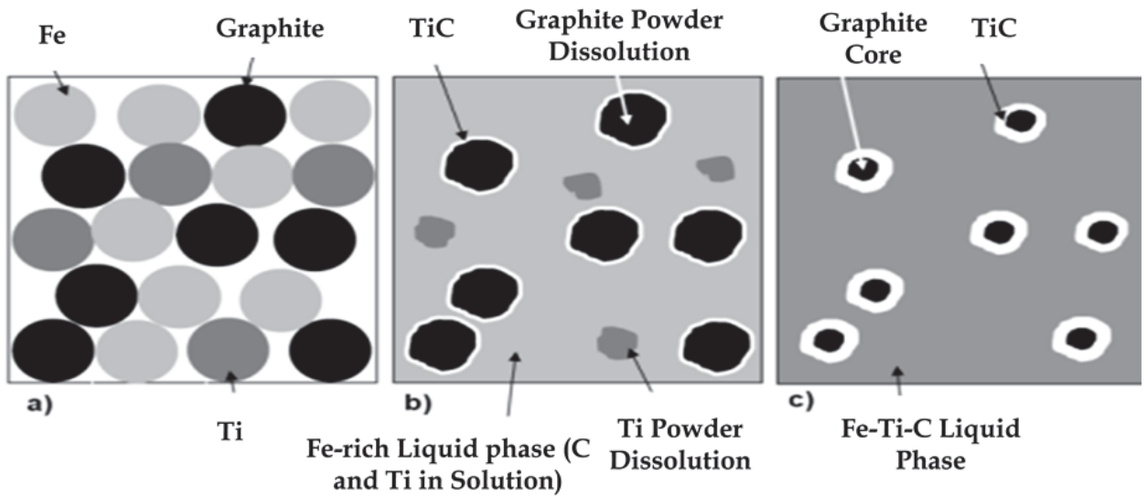

Fig. 8. TiC formation mechanism

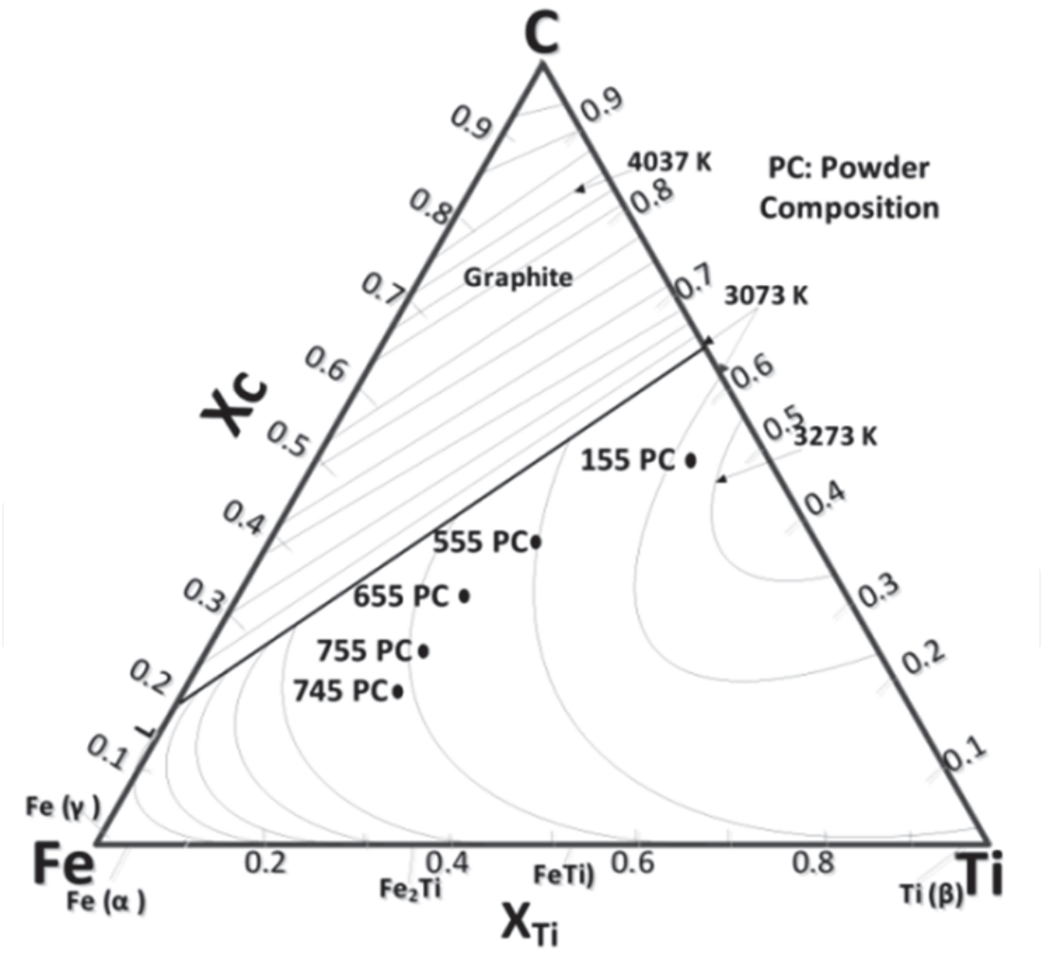

Fig. 9. Liquid projection

Fig. 10 confirms that there is a large phase field where both liquid and solid TiC will exist in a semi-solid state. It also confirms that Fe-rich mixtures (e.g., the left-hand side of the diagram) have lower liquidus temperatures. Dilution with the substrate increases the Fe content in the clad, thereby decreasing the liquidus temperature. Dilution thus plays a crucial role in establishing the clad microstructure and TiC morphology.

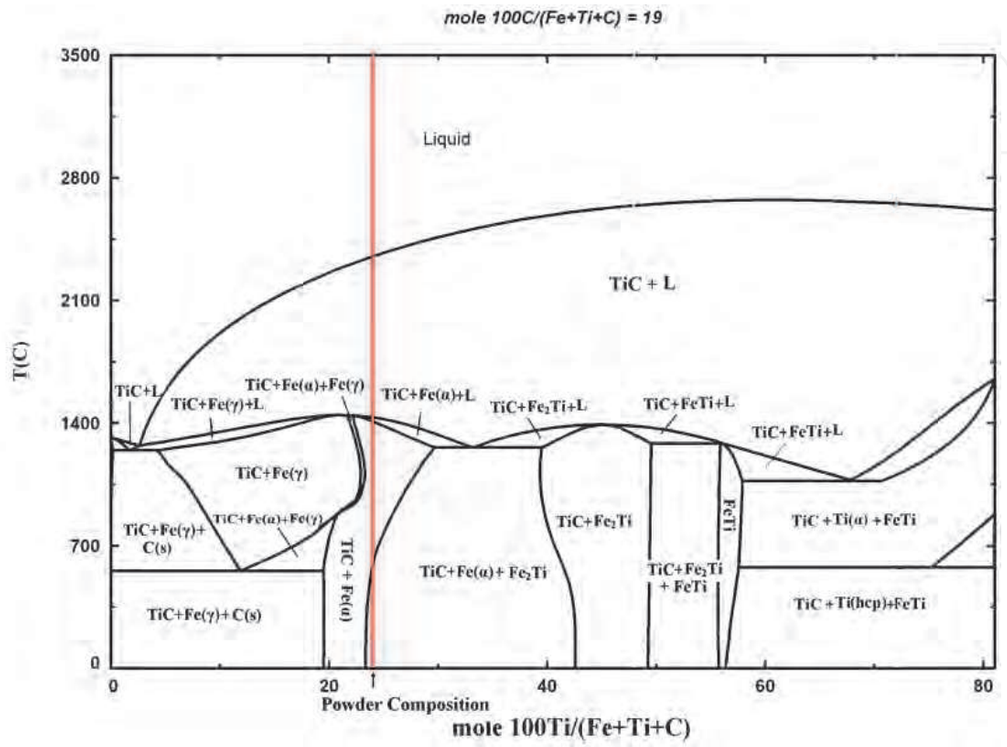

Fig. 10. Cross section of Fe-Ti-C ternary diagram in 19%at C

4. Effect of combined parameters on TiC morphology and clad microstructure

In this section, the effect of laser parameters on TiC morphology is studied. Results show that laser parameters play a crucial role in the morphology of TiC. Dendritic or spherical TiC particles with different distributions are observed, depending on the applied laser parameters. Two combined parameters, effective energy and powder deposition density, are used in order to study the effect of laser process parameters on TiC morphology.

A series of experiments are conducted in constant laser power and scan speed, constant effective energy and constant powder deposition density in order to study the TiC morphologies. Laser parameters are selected in order to be in a high quality zone as well as to result in particular values for combined parameters (namely, effective energy and powder deposition density). These series of samples help to confirm the high quality zone (e.g., zone III) found in the previous section. Fig. 11 depicts the process map for the experiments.

Samples with powder deposition density (*PDD*) greater than or equal to 0.010 g/mm^2 were selected for detailed analysis. Low clad height was the main reason for the lack of ability to analyze the samples with low *PDD* (less than 0.010 g/mm^2).

4.1 Constant laser power with different scan speeds (type A experiments)

Two groups of samples were investigated in this section: samples A1, A2, and A3, with 961 W laser powers at a scan speed of 120, 210, and 330 mm/min (Fig. 11). The second group has 907 W laser power explored with scan speeds similar to the first group.

As observed in Fig. 12, sample A1 shows dendrites of TiC particles in the clad. Table 4 shows that sample A1 has the maximum value for E_{eff} and *PDD* among the A series of experiment. As well, it exhibits the lowest value of dilution and highest clad height amongst the three samples. In samples A2 and A3, there is no evidence of dendrites, and the TiC particles are very fine. TiC particle size in sample A2 is in the range of 1-4 μm, while sample A3 has a smaller size range.

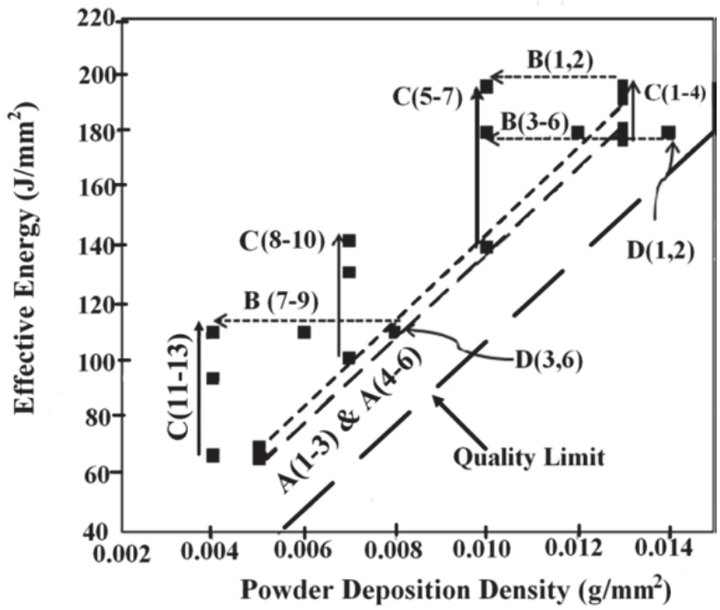

Fig. 11. Map study for groups A to D

The same trends were observed in samples A4, A5 and A6. In both groups of samples, it is noted that, by increasing the scan speed, dilution is increased, clad height is decreased, and the TiC microstructure is finer. This can be attributed to the relationship between scan speed and *PDD*. Specifically, as the scan speed increases, the *PDD* decreases. Since the laser power is constant, a larger portion of energy can be assigned for melting the substrate by decreasing the *PDD*, which then increases dilution.

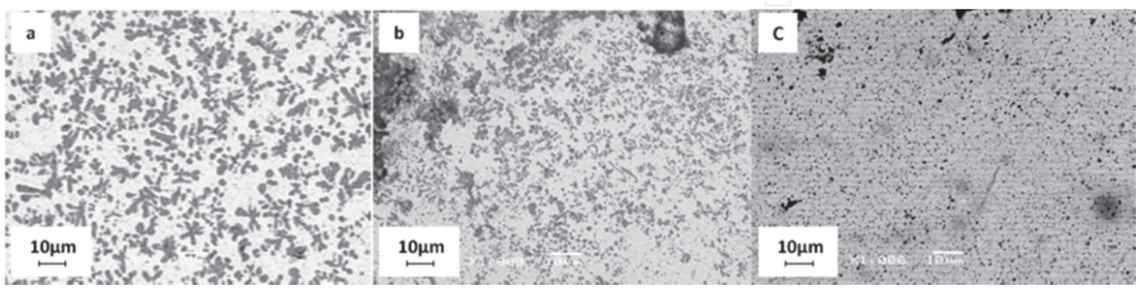

Fig. 12. Sample A1 (dendrites of TiC), b) sample A2, c) sample A3

Sample Category	Sample NO.	Laser Power (W)	Scan speed (mm/min)	Powder feed rate (g/min)	Effective Energy (J/mm^2)	Powder deposition density(g/mm^2)	Hardness (HVN)	Dilution %	Clad Height (mm)
A	1	961	120	4	192	0.013	575	72.8	1.40
	2	961	209.7	4	110	0.008	317	89.0	0.40
	3	961	330	4	70	0.005	750	94.9	0.14
	4	907	120	4	181	0.013	600	69.6	1.00
	5	907	210	4	104	0.008	400	88.0	0.10
	6	907	330	4	66	0.005	570	93.0	0.07
B	1	982	120	4	196	0.013	350	73.0	1.10
	2	982	120	3	196	0.010	650	77.0	0.60
	3	884	117	4	180	0.014	650	69.1	1.60
	4	907	120	4	181	0.013	600	69.6	1.00
	5	758.2	101.1	3	180	0.012	900	64.0	0.60
	6	589.7	78.6	2	180	0.010	2400	66.7	0.50
	7	961	209.7	4	110	0.008	317	89	0.4
	8	926.7	202.2	3	110	0.006	550	95	0.2
	9	864.9	188.7	2	110	0.004	600	--	---
C	1	884	120	4	177	0.013	650	70.3	1.60
	2	907	120	4	181	0.013	600	69.6	1.00
	3	961	120	4	192	0.013	575	72.8	1.40
	4	982	120	4	196	0.013	350	73.0	1.10
	5	700	120	3	140	0.010	850	70.0	0.90
	6	589.7	78.6	2	180	0.010	2400	66.7	0.50
	7	982	120	3	196	0.010	650	77.0	0.60
	8	506	120	2	101	0.007	644	79.0	0.07
	9	982	180	3	131	0.007	593	63.0	0.04
	10	708	120	2	142	0.007	584	75.5	0.1
	11	506	180	2	67	0.004	240	79.0	Low
	12	708	180	2	94	0.004	1000	80.0	0.14
	13	864.9	188.7	2	110	0.004	600	--	---
D	1	884	117	4	180	0.014	650	69.1	1.60
	2	663.4	88.5	3	180	0.014	1800	65.0	0.70
	3	961	209.7	4	110	0.008	317	89.0	0.4
	4	720.7	157.3	3	110	0.008	932	63.0	0.25
	5	480.5	104.8	2	110	0.008	450	88.8	0.10
	6	961	210	4	110	0.008	317	88.0	0. 40

Table 4. Results and data for groups A to D

4.2 Constant effective energy with variable powder deposition density (Type B Experiments)

The results of samples (e.g., sample B1 and B2 with 196 J/mm^2 and sample B3, B4, B5 and B6 with 180 J/mm^2) are presented in this section. Fig. 13 a-b illustrate the TiC morphology in samples B1 and B2, respectively. These samples have identical E_{eff} (i.e., 196), laser power and scan speeds, but their respective *PDD* values are 0.013 and 0.010, which result from different powder feed rates (4 and 3 g/min). This shows that sample B1 has a dendritic structure in almost the entirety of the clad, whereas sample B2 has very fine TiC particles distributed in the clad, as illustrated at Fig. 13-b.

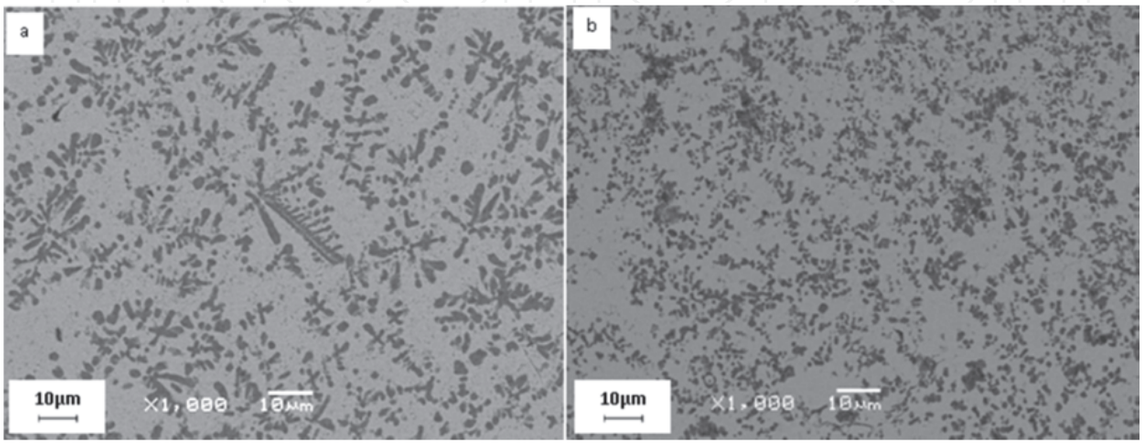

Fig. 13. BSE images for a) sample B1 and b) sample B2

Fig. 14 a-b show the clad in samples B3 and B4. These samples have different *PDD*, 0.014 and 0.013. Sample B3 with *PDD* of 0.014 shows the dendritic structure of the TiC in the clad. At the bottom of the clad, very fine TiC particles can be seen approximately 100 µm from the clad/substrate interface. Fig. 14-b also shows a dendritic structure, specifically at the middle and top of the clad in sample B4. Sample B3 shows well developed TiC dendrites compared to that of sample B4.

Fig. 14-c shows that sample B5 has fine TiC particles at the bottom of the clad (which gradually become coarser) and dendritic TiC in the middle. B5 microstructure shows both the dendritic and spherical morphology of TiC. The observed microstructure in B5 is not fully dendritic, similar to B3. However, dendrites of TiC can be observed in some locations in the middle and at top of the clad.

Fig. 14-d depicts sample B6 with a *PDD* of 0.010. TiC particles are distributed uniformly in the clad. There is no evidence for the presence of a dendritic structure of TiC particles. TiC morphology in sample B6 is spherical and the TiC particle aspect ratio can be found between 1:1 and 1:5. As Table 4 indicates, hardness values for this sample are high (e.g., 1300-3500 HVN).

This portion of the study on TiC morphology proves that *PDD* plays a crucial role in TiC formation and on the observed morphology of TiC particles. A considerable difference in TiC morphology can be detected for samples B1 and B2 which have identical laser parameters and E_{eff}, but different *PDD*, resulting from varying powder feed rate. The same can be said for the B3 to B6 series of data.

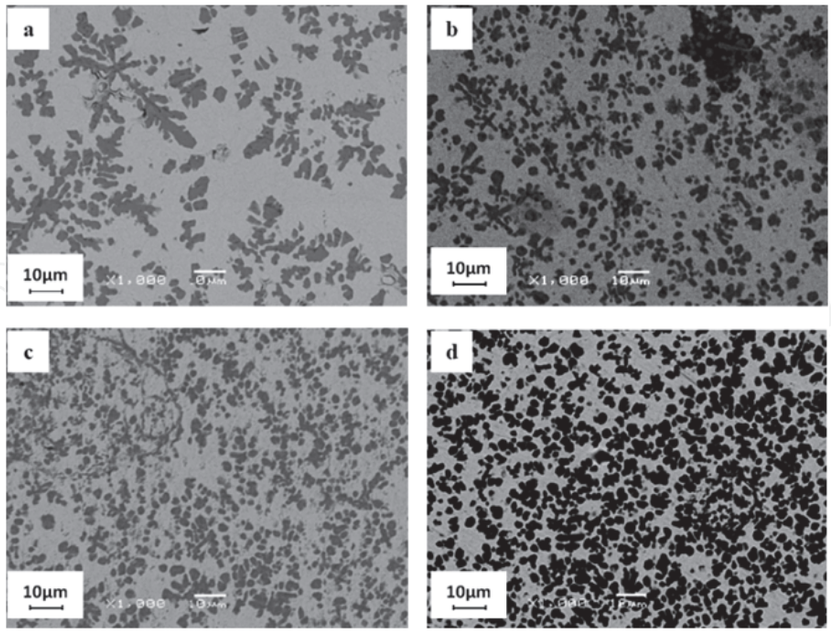

Fig. 14. a) Sample B3 b) sample B4 c) sample B5 d) sample B6

4.3 Constant powder deposition density with variable effective energy (experiments series C)

In this section, TiC particle morphology resulting from a constant powder deposition density with varying E_{eff} was studied. For this purpose, a series of samples which are identical in *PDD* and different in E_{eff} are selected. Samples C1 to C4 in the first group and C5 to C7 in the second group were investigated.

In the first group (C1 to C4), the scan speed and powder feed rate are constant. Therefore, laser power is the only parameter that is variable to create a different E_{eff}. All the samples show a dendritic structure for the TiC particles. An E_{eff} range of 177 to 196 does not have a considerable effect on TiC morphology with a constant *PDD* (0.013). Table 4 shows little change in dilution for this series of samples. Since all the parameters (except laser power) are the same, it can be seen that in the range of 884 to 982 W, these parameters form a dendritic structure.

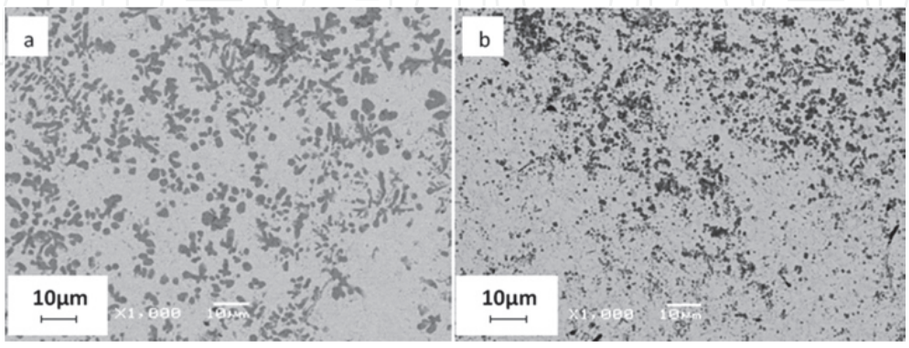

Fig. 15. BSE image of TiC morphology resulting from different *PDD* a) sample C4 b) sample C7

Thus, it may be concluded that with constant powder deposition density and laser parameters (such as scan speed, powder feed rate), increasing the E_{eff} (i.e., increasing the laser power) likewise increases the probability of creating a liquid melt pool. As a result, the TiC particle structure is mostly dendritic. This interpretation is applicable to the first group of samples (C1 to C4).

Observing samples C5 and C7 provides valuable information. Other than for the laser power, they have the same laser parameters. Sample C5 has a lower laser power (700) than sample C7 (982). From the clad microstructures, it can be seen that dendritic TiC can be detected in sample C5 whereas sample C7 shows very fine TiC particles but no evidence of a dendritic structure. Higher laser power can cause increased dilution, which changes the clad composition to the Fe-rich side and precludes dendrite formation due to the small freezing range, as shown at the left side of the phase diagram.

4.4 Identical effective energy and powder deposition density (experiment series D)

The purpose of this section is to clarify the effect of identical effective energy and powder deposition density on the morphology of the TiC particles formed during in-situ laser cladding. As mentioned earlier, the process parameters have been calculated to be in the high quality clad zone and also resulted in a specific effective energy and powder deposition density. Table 4 shows that sample D1 and D2 have the same effective energies (E_{eff}) and powder deposition densities (*PDD*), but dissimilar process parameters. The same situation can be seen in samples D3, D4, D5 and D6. Laser conditions of D1 and D2 have been used later in powder composition study (i.e. conditions A and B, respectively).

Fig. 16-a illustrates back scatter images of sample D1 where dendritic TiC can clearly be seen. Conversely, Fig. 16-b illustrates the TiC morphology for sample D2, and no evidence of a dendritic structure for TiC can be found. Moreover, the distribution of TiC particles in the clad is very uniform compared to sample D1. A simple comparison between Fig. 16-a and 17-b shows there is a considerable difference between TiC morphology, although both have the same E_{eff} and *PDD* values. Both samples (D1, D2) show fine TiC at the clad bottoms which gradually becomes coarser at the top of the clad.

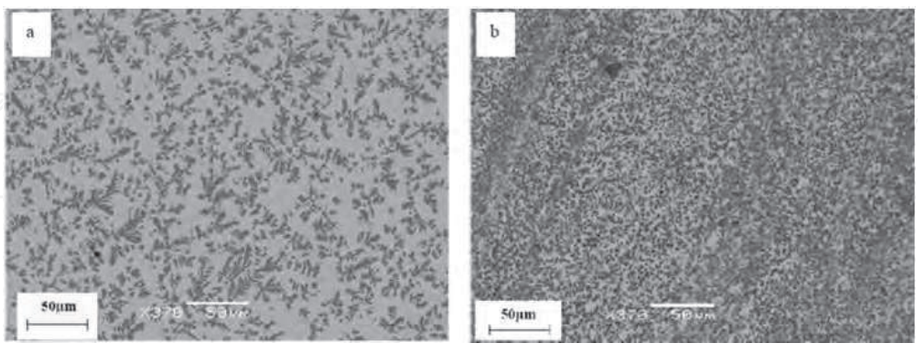

Fig. 16. TiC morphology of samples a) D1 and b) D2

4.5 Discussion

In order to create a metallurgical bond between the clad and the substrate, dilution must occur. Fig. 9 shows that dilution by Fe decreases the liquidus temperature of the melt pool (labeled dot). Fig. 10 illustrates a vertical section through the ternary Fe-Ti-C phase diagram

at a constant composition of 19%at C using the Factsage software. According to the Fe-Ti-C ternary diagram, depending on the melt pool temperature (conditional on laser process parameters), ternary liquid can be present either in a single phase or in equilibrium with TiC/C to form a semi-solid melt pool. In a semi-solid melt pool, TiC and liquid are in equilibrium, as is shown in Fig. 10. Further, a semi-solid melt pool resulted from a peak temperature less than the liquidus temperature, and spherical TiC particles which are distributed uniformly or in clusters can form from this mechanism.

In contrast, if the peak temperature exceeds the liquidus temperature, a liquid melt pool can be formed. Therefore, according to Figure 13a, TiC dendrites are the first phase to solidify during cooling and create dendritic TiC.

Fig. 16 depicted different microstructures for samples D1 and D2. Sample D1 contains dendritic TiC, whereas sample D2 shows spherical TiC particles which are distributed in the matrix. Since the E_{eff} and *PDD* are identical for both, the only reason for the dissimilar microstructure could be the laser parameters, specifically the laser power. According to Fig. 9, dilution with Fe decreases the liquidus temperature. Peak power (i.e., 884) increases the melt pool temperature and thus increases the probability of having a liquid melt pool. Hence, the clad microstructure exhibits a well-developed dendritic structure of TiC.

In sample D6, although a higher laser power has been applied compared to sample D1 (i.e., 961), a dendritic TiC could not be detected. The diagram confirms that there is a large region in which liquid and solid TiC can be in equilibrium. This region decreases by increasing the Fe content. Therefore, in samples D4 and D6 (which have lower powder deposition density [i.e., 0.008]), dilution plays a vital role. The clad composition increases in Fe, and dendritic structures of TiC did not develop during solidification. On the other hand, Fig. 10 shows that by increasing the Fe content by dilution, the freezing range decreases. By decreasing the freezing range, the chance of dendrite formation decreases. This phenomenon can explain the TiC morphology in C5 and C7. Dendrites of TiC were observed in C5 with a laser power of 700 W, whereas no evidence of dendritic TiC was observed in sample C7 with a laser power of 900 W.

In laser cladding, powder and substrate absorbed the energy in order to melt and create the clad. By increasing the powder feed rate, the energy portion absorbed by the powder increases, allowing for a decrease in laser energy absorbed by the substrate. As a result, dilution with the substrate is decreased. Increasing the laser power, or increasing the scan speed, increases the contribution of dilution (as seen in Table 4). By comparing samples D1 and D2, it can be seen that dilution in sample D1 is higher than sample D2.

By increasing the dilution amount, the liquidus temperature decreases and shifts the clad composition to the Fe-rich side of the phase diagram. This results in a change in microstructure of the clad and TiC morphology.

Several modelling techniques have been used to model laser cladding by powder injection. These help to illustrate the physics of the process. A review of the attenuation of laser power in different powder feed rates and nozzle angles were presented, and the temperature distribution in the substrate and the powder particles on the substrate's surface was calculated (Huang, 2005).

5. Powder composition study

In this section, the effect of powder composition on TiC morphology and clad hardness using the in-situ laser cladding process was studied. Two atomic ratios, 45:55 and 55:45,

were selected for C:Ti (Fig. 1), the first one of which has the potential to form near stociometric TiC, while the second potentially forming residual graphite which may be beneficial from a wear perspective.. Fe percentages were explored with 70, 60, 50 and 10wt% to increase the volume fraction of TiC in the clad (Table 1). Table 5 shows the selected laser parameters for deposition as a function of composition. Note that, for samples 155, the powder feed rates were decreased, compared to the more Fe rich compositions, in order to achieve a bonded clad. Any feed rate higher than that reported in Table 5 did not create metallurgical bonding between the clad and substrate.

Parameters condition	Sample No	Laser power W	Scan speed (mm/sec)	Powder feed rate (g/min)	Effective Energy (J/mm²)	Powder deposition density (g/mm²)
A	745, 755,655,555	884.2	117	4	180	0.014
B	745, 755,655,555	663.4	88.5	3	180	0.014
A	155	884.2	117	2.12	180	0.007
B	155	663.4	88.5	0.95	180	0.004

Table 5. Applied laser parameters

5.1 SEM, EDS and image analysis results

In this section, clad microstructures of samples with different clad compositions are studied. Fig. 17 shows the SEM images of samples with identical laser parameters but different chemical compositions. Results show that clad composition affects the clad microstructure and morphology. Fig. 17-a and 18-b are related to the samples which are identical in Fe weight percentage but different in C:Ti ratio. Fig. 17-a shows the dendiritic microstructure of TiC, while Fig. 17-b depicts the spherical TiC distributed uniformly in the matrix. Decreasing the Fe percentage in the powder composition and increasing the C:Ti ratio increases the probability of a reaction between Ti and C and thus increases the volume fraction of TiC.

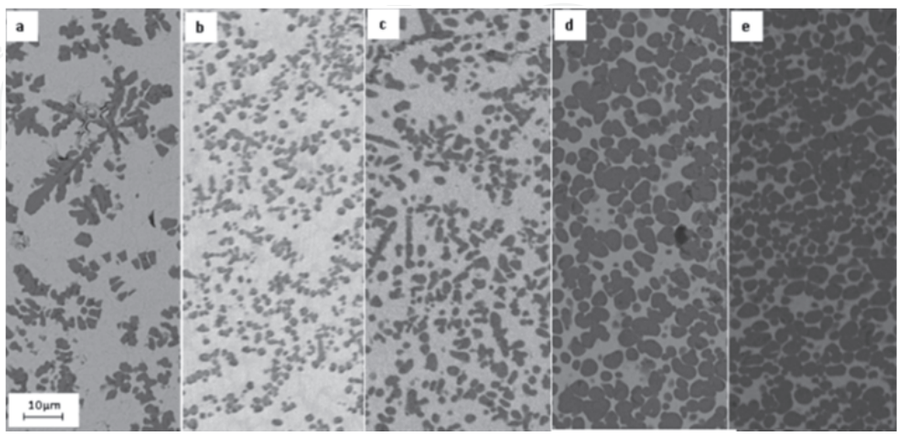

Fig. 17. Developed TiC morphologies using laser condition A for compositions of: a) 745 b) 755 c) 655 d) 555 e) 155

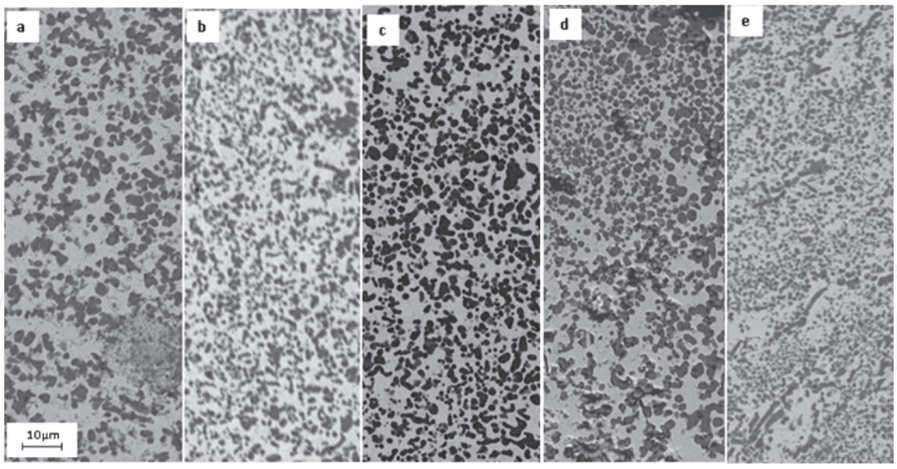

Fig. 18. Developed TiC morphologies using laser condition B for compositions of: a) 745 b) 755 c) 655 d) 555 e) 155

Fig. 17-b to 18-d show a higher volume fraction of TiC distributed in the clad. Except for sample 745-A, dendritic TiC cannot be observed in the rest of the samples. This trend also can be observed in samples deposition using condition B, as indicated in
Fig. 18. Fig. 17 and
Fig. 18 show that by decreasing the Fe percentage and increasing the C:Ti ratio, the volume fraction of TiC increases. Moreover, in condition B, dendritic TiC cannot be observed in sample 745-B and the size of the TiC particles are generally smaller for condition B compared to condition A. Image analysis helps to measure the trend of volume fraction qualitatively. Table 6 depicts the image analysis results. It can be seen that in similar applied laser conditions, the volume fraction of TiC increases by decreasing the Fe percentages. It is clear that decreasing the Fe content increases the TiC volume fraction but that this feature is more significant in laser condition A.

Sample	%Matrix	%TiC	Sample	%Matrix	%TiC
745-A	81	19	745-B	56	44
755-A	69	31	755-B	63	37
655-A	66	34	655-B	50	50
555-A	43	57	555-B	54	46
155-A	30	70	155-B	45	55

Table 6. Image analysis results

5.2 Hardness results

Hardness results are depicted in
Fig. 19, which provides information about samples with different chemical compositions deposited by laser condition A. Each hardness value is an average of at least three measurements at an identical position from the clad/substrate interface. It can be seen that, by decreasing the Fe percentage, general hardness values are increased. Sample 155-A with a minimum Fe percentage shows the highest clad hardness. This trend can also be seen in samples deposited by condition B.

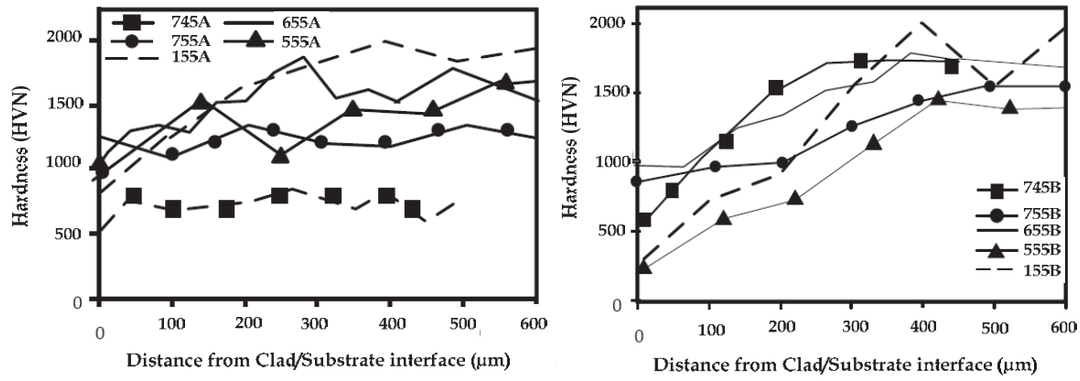

Fig. 19. Hardness profile for samples deposited with laser condition A, B

Fluctuation in hardness results normally happens in composites because of different hardness values of matrix and reinforcement particles. Moreover, an average of three measurements can be a source of fluctuation depending on which phase is punched by the indenter. Sample 745-A with dendritic TiC has the lowest fraction of TiC particles (as illustrated in Fig. 17-a and Table 6), causing a generally lower hardness compared to the other samples. Deposition of the same composition (sample 745-A) under different laser conditions (i.e., sample 745-B) increases the hardness profile dramatically. The main reason for hardness enhancement is the different distribution and morphology of TiC particles in 745-A compared to those in 745-B, which also significantly increases the TiC volume fraction from 19 to 44%.

5.3 Discussion

The temperature and composition of a clad melt pool during deposition are two main factors that affect final clad microstructure and TiC morphology. Laser power establishes the peak power that determines the clad temperature. Depending on the clad position, different cooling and solidification rates are developed which affect the clad microstructure and carbide morphologies. Composition is affected by initial fed powder composition and the extent of dilution by the Fe-rich matrix. Fig. 9 shows the liquidus projection in a ternary phase diagram of Fe-Ti-C. If no dilution by the substrate is assumed, then it is possible to state that the liquidus temperature of the powder mixture is about 2618 K (2345 °C) in a powder composition of 745 and the liquidus temperature of composition 155 is about 3384 K (3111°C). Thermal modelling of A and B laser conditions shows peak temperatures of 2200°C and 1831°C, respectively (Emamian, 2010d). Only sample 745A exhibits a dendritic TiC morphology arising from solidification of a completely liquid melt pool. This indicates that the laser peak temperature exceeded the liquidus temperature of the clad composition. The main reason for the formation of a complete liquid melt pool in this sample is dilution by the substrate which shifts the clad composition to the Fe-rich side of Fig. 10, resulting in a decrease in the liquidus temperature. In the rest of the samples, as Fig. 9 shows, increasing the C:Ti ratio and decreasing the Fe percentage in the powder mixture, causes an increase in the liquidus temperature. Therefore, the peak temperature developed by the laser heating does not exceed the liquidus temperature for the clad composition. Therefore a full liquid melt pool does not develop and spherical TiC particles are formed from the semi solid melt pool. While samples 745-A and 755-A have very close chemical compositions, differences in liquidus temperatures result in a considerable change in TiC morphology.

6. Wear

Wear resistance is an important function in the balance of properties of metal matrix composites. Wear starts from softer components which are in contact with counterfaces (i.e., pin, abrasive material or steel ball). Therefore, in metal matrix composites with hard particles, the matrix is worn in the preliminary stages of the wear process. Different mechanisms of matrix degrading such as plastic deformation, micromachining, crack propagation and brittle chipping, which are controlled by the matrix mechanical properties (i.e., hardness or fracture toughness) can increase the wear rate.

Wear can usually be classified on the basis of the nature of interactions, such as two-body or three-body. For two-body abrasive wear, a delamination model is feasible. In this model, wear resistance strongly depends on fracture toughness and not on composite strength, because crack propagation is the controlling factor. In three-body abrasive wear, abrasive particles tend to break down and bury themselves in alloys with relatively soft matrices. However, hard particles in composites resist scratching because of their high hardness under low loads and crack into small pieces under heavy loads. The broken particles remain embedded in the matrix during wear. In this case, composite strength and fracture toughness both play important roles (Jahanmir et al., 1976; Saka et al. 1985).

In this section, the wear resistances of six samples with different chemical composition deposited using two laser parameters (i.e., A, B) are studied. The objectives of this section are:

1. to find the optimal micro-structure (resulting from the laser process parameters and powder composition) of TiC in an Fe matrix with respect to the highest wear resistance ;
2. to measure the wear properties of in-situ deposited Fe-TiC by laser cladding; and
3. to find the optimal operating parameters of laser cladding that develop the best wear properties.

The wear resistance of samples is measured based on standard ASTM G65-04 using an adjusted volume loss (mm^3), as below:

$$\textit{Volume loss } (mm^3) = \textit{weight loss } (g)/\textit{density of coating } (g.cm^{-3}) * 1000 \quad (5)$$

$$\textit{Adjusted volume loss } (mm^3) = \textit{measured volume loss } (mm^3) * 228.6\ (mm)/\textit{wheel diameter after use } (mm) \quad (6)$$

6.1 Results

In the previous section, Fig. 17 and
Fig. 18 showed the TiC morphology resulting from different powder compositions and laser process parameters. In this section, wear properties of Fe-TiC composite coatings with different morphology are studied. Fig. 17 and
Fig. 18 show the distribution of TiC; however, the size of the particles and volume fraction are different.

The micro-hardness profile of conditions A and B show that samples 155A and 155B have a higher hardness value, which primarily have results from a higher volume fraction of the clad's TiC particles. In addition, sample 745A shows the lowest profile among the other samples. In considering Fig. 17, it can be concluded that a larger area of the matrix remained without the support of TiC particles. Fig. 20 illustrates the wear test results based on ASTM G65-04.

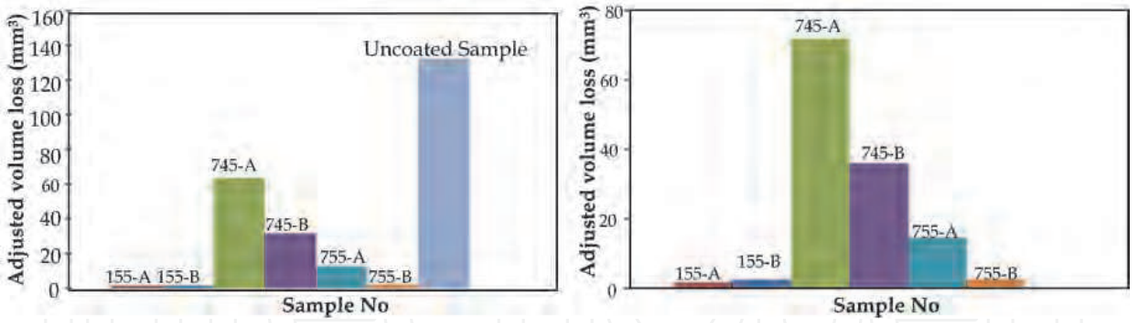

Fig. 20. Wear test results

The maximum volume loss after the uncoated sample (AISI 1030) belongs to sample 745A, while samples 155A and B have a minimum volume loss. Fig. 20 shows that by increasing the C:Ti ratio in samples, volume loss decreases. By comparing samples 745 and 755 in both conditions A and B, group 755 shows better wear resistance. Moreover, although 755B has 70%wt Fe, the results show that it has good wear resistance compared to group 155. By comparing hardness and wear test results, it can be seen that samples with higher hardness show higher wear resistance.

6.2 Discussion

By increasing the C:Ti ratio from 45:55 at% and 55:45 at% with the same laser condition, the TiC particles' morphology was formed into spherical shapes with a uniform distribution. Group 155A has a higher volume fraction of TiC compared to the 155B conditions (Table 6). By considering the melting points of ingredients (3400, 1670, and 1535° C for C, Ti and Fe, respectively), higher amounts of C and Ti in group 155 absorb a considerable portion of the laser energy compared to 745 or 755 group composition. Hence, the higher laser power in sample 155A compared to 155B encourages a reaction between C and molten Ti by the quick melting of Ti and Fe. However, in 155B, the laser energy is not sufficient to promote TiC formation in the clad. By comparing Fig. 17-c and
Fig. 18-c, it can be seen that the volume fraction and size of the TiC particles are larger in 155A than in 155B, resulting in less volume loss in 155A. Also, the larger TiC particle size in 155A compared to 155B can be another reason for better wear resistance in 155A than in 155B.
In sample 755A, a higher laser beam energy melts the substrate and increases the dilution. Hence, the volume fraction of the TiC decreases compared to 755B. Therefore, laser parameters can be selected based on powder composition in order to have a maximum TiC volume fraction.
Fig. 20 depicts how the abrasive wear performance of samples is affected by the volume fraction of TiC particles. The volume fraction of TiC particles in reverse is related to the distance between carbides occupied by the Fe matrix. It is obvious that, in abrasive conditions, the softer part is removed by grits. Therefore, it is expected that by increasing the volume fraction of the coating, the wear resistance increases (He et al., 2009; Nurminen et al., 2009; Pu, 2008). The volume fraction in this research is increased firstly by increasing the C:Ti ratio in the constant Fe percentage and secondly by decreasing the Fe percentage in the powder composition. Optimal results for wear resistance of in-situ Fe-TiC can be found in group 155A. Since Ti can dissolve in Fe during the laser cladding process, nominal 90%

TiC (93%vol TiC) is not achieved during the process; however, maximum 70% volume fraction of TiC shows considerable wear resistance.
The usual mechanism of abrasives in wear tests are grooving, plastic deformation and fracture of hard phases. Table 7 provides information about size and hardness values of hard-phase particles and abrasives.

Particle	Size range, μm	Hardness (HVN)
TiC	1-7	3200
Abrasive	212-300	1160

Table 7. Particle size information

Abrasive grits first start deforming the Fe matrix, which is the softer component in the composite coating. If the carbide interlock is sufficiently high, the exposure of the soft matrix to the abrasive will be decreased. Since the hardness of the TiC is higher than abrasives (Table 7), carbide damage is less than for grits. Moreover, in-situ TiC particles are developed during the laser cladding process, and hence the TiC/Fe interface has a strong bonding. Therefore, the probability of deboning and crack formation in the particle/binder interface decreases. Pulling out and crushing the WC particles are the main problems that have been noted by researchers (Stachowiak, G. B. & Stachowiak G.W, 2010). Furthermore, identical wear test conditions were conducted on sample WC-12%Ni (with 80%vol WC) to compare it with 155A (with 80% vol TiC). Results show a similar adjusted volume loss for both (i.e., 1.9744 and 1.7731 mm^3 volume loss for WC and 155A, respectively).

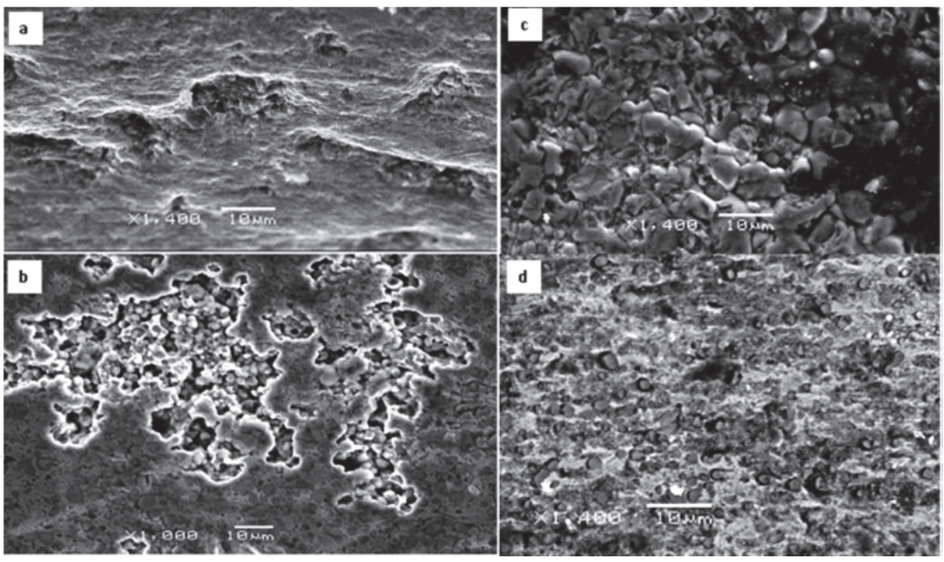

Fig. 21. (a) Plastic deformations in worn surface of 745A (b) Pulling out of carbides in worn surface of 755A (c) Worn matrix and remaining TiC particles in sample 155A (d) Worn matrix and remaining TiC particles in sample 755B

It is normal that the matrix of sample 745A, which has minimum support of the TiC, contains more plastic deformation than the others (Fig. 21 a). Matrix plastic deformation increases the stress on TiC particles, pulling them off the surface. It is worth noting that, during the wear test, increasing the temperature in the matrix around the TiC particles helps

to drop the yield stress of the matrix, resulting in easier plastic deformation around the carbides. By increasing the volume fraction of the TiC in samples 755 and 155, plastic deformation could not be observed. However, in some areas of 755A, a pulling out of the TiC is detected. Fig. 21 b shows a pulling out of the carbides in sample 755A. Group 155 shows a uniform worn surface without carbide removal. The higher volume fraction of the TiC results in the minimizing of the plastic deformation and removing of the matrix. However, volume loss still belongs to the matrix area. Fig. 21-c shows the interlocked TiC and a small area of worn matrix in 155A. Fig. 21-d depicts the worn matrix for sample 755B with the remains of the TiC. Although sample 755B contains 70% Fe, the uniform distributed particles and high volume fraction of the TiC resulted in higher wear resistance than that of 755A and 745A and B.

7. Conclusion

From the above experiments, we can conclude that two important factors – temperature and chemical composition of the clad – establish clad microstructures. We can also conclude that laser process parameters play a crucial role in the quality and microstructure of the clad, the ternary phase diagram of Fe-Ti-C can be used to predict the final microstructure of the clad. Furthermore, the melt pool chemical composition defines the liquidus temperature. Hence, the clad temperature can be higher or less than the liquidus temperature in different locations of the clad. Therefore, depending on clad and liquidus temperatures, the melt pool would be semi-solid or liquid, which defines the TiC formation mechanism and morphology.

The experiments also showed that, depending on powder deposition density (resulting from the powder feed rate and scan speed) and peak power of the clad temperature, different TiC morphologies and distributions could result. Moreover, identical combined parameters do not guarantee identical TiC morphology, as laser parameters still play a role in TiC morphology.

Furthermore, a uniform distribution of spherical TiC particles indicates that increasing the fraction of carbides in a matrix results in higher values for hardness (sample D2). From this, it can be concluded that, in order to enhance the clad hardness and wear resistance and achieve uniform carbide distribution, laser parameters must be adjusted to form a semi-solid melt pool instead of a liquid molten pool. A liquid melt pool forms dendritic TiC particles, which are not well distributed through the clad. Hence, a considerable region of clad cannot be supported by TiC particles. This conclusion also was confirmed by wear resistance results in a series of chemical composition and two laser conditions.

8. References

Ariely, S., Shen, J., Bamberger, M., Dausiger, F. & Hugel, H. (1991). Laser surface alloying of steel with TiC. *Surface and Coatings Technology,* 45 403-408.

Cui, C., Guo, Z., Wang, H. & Hu, J. (2007). In situ TiC particles reinforced grey cast iron composite fabricated by laser cladding of Ni–Ti–C system. Journal of Materials Processing Technology, 183, 380-385.

Das, K., Bandyopadhyay, T. K. & Das, S. (2002). A review on the various synthesis routes of TiC reinforced ferrous based composites. Journal of Materials Science 37, 3881-3892.

Dubourg, L. & St-Georges, L., Optimization of laser cladding process using Taguchi & EM methods for MMC coating production (2006). Journal of Thermal Spray Technology 15, 790-795

Du, B., Li, Q., Wang, X. & Zou, Z. (2007). In situ synthesis of TiC-VC particles reinforced Fe-based metal matrix composite coating by laser cladding. Hanjie Xuebao/Transactions of the China Welding Institution 28, 65-68.

Du, B., Zou, Z., Wang, X. & Li, Q. (2007). In situ synthesis of TiC-TiB2 reinforced FeCrSiB composite coating by laser cladding. Surface Review and Letters 14, 315-319.

Emamian A., Corbin, S. F. & Khajepour,A. (2010). Effect of laser cladding process parameters on clad quality and in-situ formed microstructure of Fe–TiC composite coatings. Surface and Coatings Technology 205, 2007-2015.

Emamian A., Corbin, S.F, & Khajepour A., (2010). "Study on Laser Parameters Effect on Morphology of In-Situ Fe-TiC particles Deposition on Mild Steel Using Laser Cladding Process" ICALEO Conference 2010, Anheim, California, USA.

Emamian, A., Corbin, S.F, & Khajepour A., (2010). "Correlation between temperature distribution and formed microstructure of in-situ laser cladding of Fe-TiC on carbon steel" ICALEO Conference 2010, Anheim, California, USA.

Emamian A., Corbin, S.F., & Khajepour A. (2009). "In-situ TiC particles reinforced carbon steel composite Fabricated by laser cladding of Fe-Ti-C system", 21st Canadian Material Science Conference, Kingston, Canada.

He, Q., Wang, Y., Zhao, W. & Cheng, Y. (2009). Interface microstructure and wear properties of TiC-Ni-Mo coatings prepared by in-situ fabrication of laser cladding. Hanjie Xuebao/Transactions of the China Welding Institution 30.

Hirokai Okamoto, (2000). Phase Diagrams for Binary Alloys (ASM)

Huang Y.L (2005). Interaction between laser beam and powder stream in the process of laser cladding with powder feeding. Journal of Modeling and simulation in material science and engineering 13, 47-56.

Jahanmir S., Abrahamson E.P., and Suh N.P., (1976). Wear, Vol 40, p. 75.

Jiang, W. H., Fei, J. & Han, X. L. (2000). In situ synthesis of (TiW)C/Fe composites. Materials Letters, 46, 222-224.

Jiang, W. H. & Kovacevic, R. (2007). Laser deposited TiC/H13 tool steel composite coatings and their erosion resistance. Journal of Materials Processing Technology, 186, 331-338.

Nurminen, J., Näkki, J. & Vuoristo, P. (2009). Microstructure and properties of hard and wear resistant MMC coatings deposited by laser cladding. International Journal of Refractory Metals and Hard Materials 27, 472-478.

Pu, Y. (2008). Microstructure and tribological properties of in situ synthesized TiC, TiN, and SiC reinforced Ti_3Al intermetallic matrix composite coatings on pure Ti by laser cladding. Appl. Surf. Sci. 255, 2697-2703.

Saka N. and Karalekas D.P., (1985). Friction and Wear of Particle Reinforced Metal-Ceramic Composites, Wear of Materials, p 784.

Stachowiak, G. B. & Stachowiak, G. W. (2010). Tribological characteristics of WC-based claddings using a ball-cratering method. International Journal of Refractory Metals and Hard Materials 28 95-105.

Tassin, C., Laroudie, F., Pons, M. & Lelait, L. (1995). Carbide-reinforced coatings on AISI 316 L stainless steel by laser surface alloying. Surface and Coatings Technology, 76-77, 450-455.

Wang, X. H., Song, S. L.& Qu, S. Y. & Zou, Z. D. (2007). Characterization of in situ synthesized TiC particle reinforced Fe-based composite coatings produced by multi-pass overlapping GTAW melting process. Surface & Coatings Technology ,201, 5899-5905.

Wang, X. H., Zhang, M., Liu, X. M.& Qu, S. Y. & Zou, Z. D. (2008). Microstructure and wear properties of TiC/FeCrBSi surface composite coating prepared by laser cladding. Surface and Coatings Technology, 202, 3600-3606.

Wang, X. H., Qu, S. Y., Du, B. S. & Zou, Z. D. (2009). In situ synthesised TiC particles reinforced Fe based composite coating produced by laser cladding. Materials Science and Technology 25, 388-392.

Wu, X. & Hong, Y. (2001). Microstructure and mechanical properties at TiCp/Ni-alloy interfaces in laser-synthesized coatings. Materials Science and Engineering A 318, 15-21.

Yan, M. & Hanqi, H. (1996). In situ laser surface coating of TiC metal-matrix composite layer. J. Mater. Sci. 31, 4303-4306.

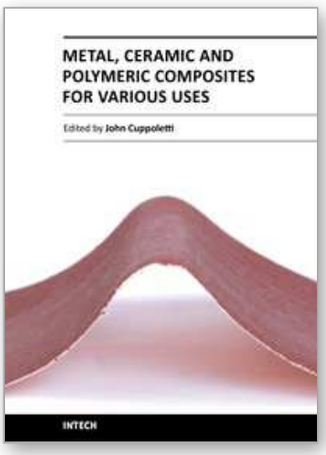

Metal, Ceramic and Polymeric Composites for Various Uses

Edited by Dr. John Cuppoletti

ISBN 978-953-307-353-8
Hard cover, 684 pages
Publisher InTech
Published online 20, July, 2011
Published in print edition July, 2011

Composite materials, often shortened to composites, are engineered or naturally occurring materials made from two or more constituent materials with significantly different physical or chemical properties which remain separate and distinct at the macroscopic or microscopic scale within the finished structure. The aim of this book is to provide comprehensive reference and text on composite materials and structures. This book will cover aspects of design, production, manufacturing, exploitation and maintenance of composite materials. The scope of the book covers scientific, technological and practical concepts concerning research, development and realization of composites.

How to reference

In order to correctly reference this scholarly work, feel free to copy and paste the following:

Ali Emamian, Stephen F. Corbin and Amir Khajepour (2011). In-Situ Deposition of Metal Matrix Composite in Fe-Ti-C System Using Laser Cladding Process, Metal, Ceramic and Polymeric Composites for Various Uses, Dr. John Cuppoletti (Ed.), ISBN: 978-953-307-353-8, InTech, Available from: http://www.intechopen.com/books/metal-ceramic-and-polymeric-composites-for-various-uses/in-situ-deposition-of-metal-matrix-composite-in-fe-ti-c-system-using-laser-cladding-process

INTECH
open science | open minds

InTech Europe
University Campus STeP Ri
Slavka Krautzeka 83/A
51000 Rijeka, Croatia
Phone: +385 (51) 770 447
Fax: +385 (51) 686 166
www.intechopen.com

InTech China
Unit 405, Office Block, Hotel Equatorial Shanghai
No.65, Yan An Road (West), Shanghai, 200040, China
中国上海市延安西路65号上海国际贵都大饭店办公楼405单元
Phone: +86-21-62489820
Fax: +86-21-62489821

IntechOpen